Ocean Sci. Discuss., 11, 1265–1300, 2014
www.ocean-sci-discuss.net/11/1265/2014/
doi:10.5194/osd-11-1265-2014

Ocean Science
Discussions
Open Access

Wave induced mixing and transport of buoyant particles: application to the Statfjord A oil spill

M. Drivdal[1], **G. Broström**[2,1], **and K. H. Christensen**[1]

[1]Norwegian Meteorological Institute, Oslo, Norway
[2]Department of Earth Sciences, University of Gothenburg, Gothenburg, Sweden

Received: 11 April 2014 – Accepted: 12 May 2014 – Published: 23 May 2014

Correspondence to: M. Drivdal (magnus.drivdal@met.no)

Published by Copernicus Publications on behalf of the European Geosciences Union.

Abstract

The modelling of wave-current and wave-turbulence interactions have received much attention in recent years. In this study the focus is on how these wave effects modify the transport of particles in the ocean. Here the particles are buoyant tracers that can represent oil droplets, plastic particles or plankton, for example fish eggs and larvae. Using the General Ocean Turbulence Model (GOTM), modified to take surface wave effects into account, we investigate how the increased mixing by wave breaking and Stokes shear production as well as the stronger veering by the Coriolis–Stokes force affect the drift of the particles. The energy and momentum fluxes as well as the Stokes drift depend on the directional wave spectrum that can be obtained from a wave model or from observations. As a first test the depth and velocity scales from the model are compared with analytical solutions based on a constant eddy viscosity (e.g. classical Ekman theory). Secondly the model is applied to a case where we investigate the oil drift after an offshore oil spill outside the western coast of Norway in 2007. During this accident the average net drift of oil was observed to be both slower and more deflected away from the wind direction than predicted by empirical models. With wind and wave forcing from the ERA Interim archive, it is shown that the wave effects are important for the resultant drift in this case, and has the potential to improve drift forecasting.

1 Introduction

An important application of upper ocean models is the mixing and drift of particles, that could represent e.g. suspended sediments, plastic particles, biological matter or oil droplets (Hackett et al., 2006). These particles are advected by the Lagrangian current that consists of an Eulerian component and the wave induced Stokes drift. To take account of both the wind and wave induced drift components, many oil drift models use an empirically based relation between the drift of an oil slick and the wind vector (James, 2002). This empirical rule can be stated as a simple equation for the drift of the

OSD
11, 1265–1300, 2014

oil, $\boldsymbol{u}_{\text{drift}}$, as a linear function of the wind vector at ten meters, $\boldsymbol{u}_{10}$, and a background ocean current, $\boldsymbol{u}_{\text{BG}}$ (Reed et al., 1994):

$$\boldsymbol{u}_{\text{drift}} = \beta \mathbf{A} \cdot \boldsymbol{u}_{10} + \boldsymbol{u}_{\text{BG}}, \quad (1)$$

where β is a constant and $\mathbf{A}$ is a rotation matrix determining the deflection of the wind induced component away from the wind direction. Typically the drift speed is about 3 % of the wind speed, giving $\beta = 0.03$, with an angle of 15° to the right of the wind direction in the Northern Hemisphere (Hackett et al., 2006). As the wind speed increases, waves will start to break at the surface and oil droplets are mixed into the water column. When a substantial portion of the oil is mixed subsurface, the mean transport rate is expected to drop to about 1 % of the wind speed with a mean direction to the right (Reed et al., 1994). During oil spills, the oil that is mixed into the ocean column will consist of a range of droplets with different rise velocities depending on e.g. size and density (Johansen, 2000). The density of the oil varies greatly due to the different oil types and the complex weathering processes that oil undergoes in the ocean (Reed et al., 1999).

An alternative to Eq. (1) is to use an ocean model to calculate the drift, but this solves only for the Eulerian component. In ocean circulation models it is common that the flux of momentum from the atmosphere is passed directly to the ocean and is related to the wind speed at 10 m through a drag coefficient. In the real ocean the wave field acts as a reservoir for momentum and energy, and a significant amount of the momentum flux from the atmosphere is taken up by the waves. The actual momentum flux received by the ocean then also depends on whether the wave field is growing, in equilibrium, or decaying. Hence, the more accurate momentum flux to use in an ocean model should be the fraction of the total flux that goes directly to the currents plus the momentum lost from the waves by dissipation (Weber et al., 2006). These sea-state dependent momentum fluxes can be calculated from the directional wave spectrum (Saetra et al., 2007; Janssen, 2012). On time scales longer than the rotational period, the Coriolis force will act on the waves and give rise to a force known as the Coriolis–Stokes force (e.g. Ursell, 1950; Lewis and Belcher, 2004; Polton et al., 2005). Directed at right angles

OSD
11, 1265–1300, 2014

to the direction of wave propagation (Northern Hemisphere), the Coriolis–Stokes force leads to an additional deflection of the current (i.e. Eulerian current), similar to the effect of the Coriolis force. In many cases the Coriolis–Stokes force can be comparable in magnitude to the standard Coriolis force, as demonstrated by Röhrs et al. (2012).

Surface wave breaking is known to enhance turbulence in the upper ocean (Craig and Banner, 1994; Agrawal et al., 1992; Gemmrich et al., 1994; Terray et al., 1996). A common way of parametrizing the influence of breaking waves in ocean models is to add a flux of turbulence kinetic energy (TKE) at the surface (Craig and Banner, 1994). The effects of wave breaking is restricted to a surface layer with a thickness on the order of the wave height (Weber, 2008). In addition to wave breaking, the waves may generate turbulence through an extra production term proportional to the shear in the Stokes drift in the TKE equation. This term can be derived using Generalized Lagrangian-mean theory (Andrews and McIntyre, 1978), as shown by Ardhuin and Jenkins (2006). However, a Stokes shear production term is also sometimes used to model the interaction of the Stokes drift with the current through a vortex force (e.g. Kantha and Clayson, 2004; Kantha et al., 2010; Janssen, 2012; Paskyabi and Fer, 2014). This vortex force gives rise to an instability, referred to as the second Craik–Leibovitch (CL2) mechanism, that causes Langmuir cells to develop (Craik, 1977). Hence on one hand we have a Stokes shear production term obtained directly in a Lagrangian reference frame, and on the other hand a similar term that parametrizes Langmuir turbulence. At present it is not clear how to to distinguish between these two mechanisms in ocean models. The inclusion of the Stokes shear production term is supported by Huang and Qiao (2010), who find that observed dissipation rates of TKE can be expressed as a function of the vertical shear in the Stokes drift. However, other observations of the dissipation rate show a better fit with the classical law of the wall scaling (Sutherland et al., 2013, 2014).

The aim of this study is to investigate the combined role of TKE injection by wave breaking, Stokes shear production, and the Coriolis–Stokes force, for the drift of buoyant particles. Here the buoyant particles have constant rise velocities, and can be

OSD
11, 1265–1300, 2014

a simple representation of oil particles or plankton such as cod eggs. The model is applied to two cases: (1) an idealized steady-state case with constant flux of momentum and energy, where the waves are represented by a theoretical spectrum, and (2) a specific case study where wind and wave data from the ERA Interim archive (Dee et al., 2011) is used as input. While the former case is well suited for studying the impact of the various wave effects, the latter case serves as a test of the model in a practical application. For the realistic case the site of the Statfjord A platform off the western coast of Norway is used, with forcing data from the time of a large oil spill that occurred in December 2007. In this case an observation of the oil slick two days after the accident indicates that the oil drifted with an average speed of about 0.5 % of the wind speed at an angle of around 90°–120° to the right.

The outline of this paper is as follows: in Sect. 2 the governing equations of motion and the turbulence closure model are presented, including the wave-induced transport and mixing parametrizations mentioned above. Also the transport equation of the particles, the model and experiment setup are described. In Sect. 3 the results from the steady state experiment (case 1), are presented and discussed. Sect. 4 presents the results when applying the model for the Statfjord A oil spill (case 2). In Sect. 5 we present some concluding remarks.

2 Formulation of the model components

In the following the x axis will be defined as eastward, the y axis northward and the z axis will be directed upwards. The velocity is given by $\boldsymbol{u} = u\hat{i} + v\hat{j} + w\hat{k}$, where $\hat{i}$, $\hat{j}$ and $\hat{k}$ denote the unit vectors in the x, y and z directions, respectively. Furthermore the Eulerian velocity $\boldsymbol{u}$ will be separated into a mean part $\overline{\boldsymbol{u}}$ and fluctuating part $\boldsymbol{u}'$. The ocean surface will be assumed to be at $z = 0$.

OSD
11, 1265–1300, 2014

2.1 Sea state dependent fluxes

Wave prediction models provide reliable forecasts of the directional wave spectra that can be used to obtain the sea-state dependent momentum and energy fluxes to the ocean. These fluxes depend on the shape of the directional wave variance spectrum F, which for deep water waves is determined by the wave energy balance equation (Komen et al., 1994):

$$\left(\frac{\partial}{\partial t} + \boldsymbol{c}_g \cdot \nabla\right) F = S_{\text{in}} + S_{\text{nl}} + S_{\text{d}}, \tag{2}$$

where $F(\omega, \theta)$ depends on the wave frequency, ω, and direction, θ, and $\boldsymbol{c}_g$ is the group velocity of the waves. The wave source terms S_{in}, S_{nl} and S_{d} represent wave growth by wind, nonlinear transfer between wave components, and wave dissipation due to wave breaking/white capping, respectively. When the wave field is known from a wave model, the release of kinetic energy from wave breaking can be calculated from S_{d} according to (e.g. Janssen, 2012)

$$\Phi_{\text{oc}} = \rho_{\text{w}} g \int_0^{2\pi} \int_0^{\infty} S_{\text{d}} \, \mathrm{d}\omega \mathrm{d}\theta \, . \tag{3}$$

If wave spectra are not available, this energy flux can be parametrized by $\Phi_{\text{oc}}/\rho_{\text{w}} = \alpha u_*^3$, where u_* is the water side friction velocity and α a dimensionless parameter. The value of α can be adjusted to include sea state dependence (Janssen, 2012), but $\alpha = 100$ is frequently used (Craig and Banner, 1994).

The momentum flux to the ocean column ($\boldsymbol{\tau}_{\text{o}}$) consists of the flux transferred by turbulence across the air–sea interface and a flux of momentum from waves due to wave breaking and white capping. Using the source terms in Eq. (2), the effective

OSD
11, 1265–1300, 2014

momentum flux into the ocean may be written as (e.g. Saetra et al., 2007)

$$\boldsymbol{\tau}_{\mathrm{o}} = \boldsymbol{\tau}_{\mathrm{a}} - \rho_{\mathrm{w}} g \int_0^{2\pi} \int_0^{\omega_{\mathrm{c}}} \frac{\mathbf{k}}{\omega} (S_{\mathrm{in}} + S_{\mathrm{d}}) \, \mathrm{d}\omega \, \mathrm{d}\theta \,, \tag{4}$$

where $\boldsymbol{\tau}_{\mathrm{a}}$ denotes the total atmospheric stress. For higher frequencies than the cutoff-frequency ω_{c}, it can be assumed that there is a balance between wind input and dissipation (Janssen, 2012), and hence this is the upper limit for the integral over frequencies in Eq. (4).

2.2 Momentum budget

For deep water waves the Stokes drift $\boldsymbol{u}_{\mathrm{S}} = u_{\mathrm{S}}\hat{i} + v_{\mathrm{S}}\hat{j}$ can be calculated, to second order in wave steepness, from the wave spectral density (e.g. Jenkins, 1989):

$$\boldsymbol{u}_{\mathrm{S}} = 2 \int_0^{2\pi} \int_0^{\infty} \omega \mathbf{k} F \exp(2|k|z) \, \mathrm{d}\omega \mathrm{d}\theta \,. \tag{5}$$

From this expression the Coriolis–Stokes force can be calculated according to $-\rho_{\mathrm{w}} f \hat{k} \times \boldsymbol{u}_{\mathrm{S}}$, where f is the Coriolis parameter. A discussion on how this force affects the mean flow can be found in e.g. Polton et al. (2005). Assuming no horizontal pressure gradients and a horizontally homogeneous ocean, the horizontal Reynolds-averaged momentum equations with the Coriolis–Stokes force read

$$\begin{aligned} \frac{\partial \overline{u}}{\partial t} &= -\nu \frac{\partial^2 \overline{u}}{\partial z^2} - \frac{\partial}{\partial z} \overline{u'w'} + f(\overline{v} + v_{\mathrm{S}}) \,, \\ \frac{\partial \overline{v}}{\partial t} &= -\nu \frac{\partial^2 \overline{v}}{\partial z^2} - \frac{\partial}{\partial z} \overline{v'w'} - f(\overline{u} + u_{\mathrm{S}}) \,, \end{aligned} \tag{6}$$

OSD
11, 1265–1300, 2014

where $\overline{u'w'}$ and $\overline{v'w'}$ are the Reynolds shear stresses, and it has been assumed that the dominant part is related to the vertical variation. Using the Boussinesq eddy viscosity assumption, the Reynolds shear stresses are given by

$$\overline{u'w'} = -\nu_t \frac{\partial \overline{u}}{\partial z}, \overline{v'w'} = -\nu_t \frac{\partial \overline{v}}{\partial z}. \quad (7)$$

The eddy viscosity ν_t is determined by the turbulence closure model, in this case the two-equation model described later on in Sect. 2.3. With the total momentum flux to the ocean given by Eq. (4), the boundary condition for $\overline{\boldsymbol{u}}$ at the surface is given by

$$\rho_w \nu_t \frac{\partial \overline{u}}{\partial z}\Big|_{z=0} = \boldsymbol{\tau}_o^{(x)}, \rho_w \nu_t \frac{\partial \overline{v}}{\partial z}\Big|_{z=0} = \boldsymbol{\tau}_o^{(y)}. \quad (8)$$

2.3 Turbulence kinetic energy (TKE) budget

Including the Stokes shear production, the TKE budget for horizontally homogeneous flow becomes (Grant and Belcher, 2009)

$$\frac{\partial k}{\partial t} = -\overline{u'w'}\frac{\partial \overline{u}}{\partial z} - \overline{v'w'}\frac{\partial \overline{v}}{\partial z} - \overline{u'w'}\frac{\partial u_s}{\partial z} - \overline{v'w'}\frac{\partial v_s}{\partial z} - \overline{w'b'} - \frac{\partial}{\partial z}\left(\overline{w'k} + \frac{1}{\rho}\overline{w'p'}\right) - \varepsilon. \quad (9)$$

Assuming that the transport term (sixth term on the right hand side of Eq. 9) can be expressed by a simple gradient transport formulation we obtain

$$\frac{\partial k}{\partial t} = \frac{\partial}{\partial z}\left(\frac{\nu_t}{\sigma_k}\frac{\partial k}{\partial z}\right) + \mathcal{P} + \mathcal{P}_S + \mathcal{G} - \varepsilon, \quad (10)$$

where σ_k is the turbulent Schmidt number. The terms $\mathcal{P}$, $\mathcal{P}_S$ and ε in Eq. (10) represent shear production (two first terms on the right hand side of Eq. 9), the Stokes shear production (third and fourth terms on the right hand side of Eq. 9) and the dissipation rate (last term on the right of Eq. 9). With the Boussinesq eddy viscosity assumption,

OSD
11, 1265–1300, 2014

the Reynolds shear stresses in Eq. (9) are given by Eq. (7). Similarly, the buoyancy production term is modeled by the eddy diffusivity ν_t':

$$\mathcal{G} = -\overline{w'b'} = -\nu_t' N^2 , \tag{11}$$

where N is the buoyancy frequency. The eddy viscosity and diffusivity are given by

$$\nu_t = c_\mu k^{\frac{1}{2}} l , \nu_t' = c_\mu' k^{\frac{1}{2}} l , \tag{12}$$

where l is the turbulence length scale and c_μ and c_μ' are the stability functions, which can either be constants or functions derived empirically or from a higher order turbulence model. In this study, the flux of TKE defined by Eq. (3) is applied as a boundary condition at the surface, thus

$$-\frac{\nu_t}{\sigma_k}\frac{\partial k}{\partial z}\Big|_{z=0} = \frac{\Phi_{oc}}{\rho_w} . \tag{13}$$

In addition to solving the TKE Eq. (10) we will here use a two-equation closure scheme that requires another prognostic equation to derive information about the turbulence length or time scale. Using the generic length scale (GLS) approach (Umlauf and Burchard, 2003), the second equation is for a generic parameter ψ:

$$\frac{\partial \psi}{\partial t} = \mathcal{D}_\psi + \frac{\psi}{k}(c_{\psi_1}(\mathcal{P} + \mathcal{P}_S) + c_{\psi_3}\mathcal{G} - c_{\psi_2}\varepsilon) , \tag{14}$$

where $\mathcal{D}_\psi$ is a gradient transport term like in Eq. (10), and c_{ψ_1}, c_{ψ_2} and c_{ψ_3} are model constants. The generic length scale ψ is related to the turbulence kinetic energy k and the length scale l through

$$\psi = (c_\mu^0)^p k^m l^n , \tag{15}$$

where c_μ^0 is the constant value of the stability function c_μ in the log-layer (Umlauf and Burchard, 2003). For appropriate choices of the exponents p, m, and n, the variable ψ

OSD
11, 1265–1300, 2014

can be directly identified with the classic length-scale determining variables, such as in the k–ε, k–ω or k–kl models (e.g. Warner et al., 2005).

Following Umlauf and Burchard (2003), the value of the mixing length at the surface is given by

$$l(z = 0) = L z_0 , \tag{16}$$

where L and z_0 are constants and the source of turbulence from breaking waves has been assumed to be at $z = 0$. When the length scale at the surface is given by Eq. (16), a Dirichelet boundary condition for ψ can be derived from Eq. (15). Craig and Banner (1994) use the surface roughness for z_0 and that $L = \kappa \sim 0.4$ in Eq. (16). However, it is pointed out by Umlauf et al. (2003) that $z_0 = l/L$ at $z = 0$ is not related to any kind of surface roughness length, rather, it is connected to the length scale of injected turbulence, which is determined by the spectral properties of turbulence at the source. Umlauf et al. (2003) suggest a value of L that is smaller than κ. Different values of L and z_0 can be found in the literature. As discussed by Rascle et al. (2012), parametrization of wave breaking through a flux boundary condition as in Eq. (13) is often accompanied by a large prescribed downward diffusion (by specifying values of z_0) in order for TKE to penetrate deep enough. Rascle and Ardhuin (2009) use $z_0 = 1.6H_S$ and a prescribed length scale $l = \kappa(z_0 - z)/(1 + \kappa(z_0 - z)/h)$, where H_S is the significant wave height of the wind sea and h is the mixed layer depth.

In the context of two-equation turbulence closure models, values of z_0 are usually somewhat smaller. While e.g. Umlauf et al. (2003) and Saetra et al. (2007) use that $z_0 = H_S$, Carniel et al. (2009) use a Charnok-type expression to describe z_0. Jones and Monismith (2008) find the best match with observations to be $z_0 = 1.3H_S$. However, Jones and Monismith (2008) use data from an area with shallow water and wave heights smaller than for typical open ocean conditions (notably, for the Statfjord A case we have H_S up to 4.5 m). Based on results from fine structure temperature measurements (Gemmrich and Farmer, 1999), Gemmrich and Farmer (2004) use that $z_0 = 0.2$ m for wave conditions where $H_S = 3.5$ m, which is more representative for the

OSD
11, 1265–1300, 2014

conditions during the Statfjord A oil spill. We propose that instead of calculating the mixing length scale at the surface through values of z_0, we can use the information from the wave spectrum directly. In addition to the energy flux Φ_{oc}, the wave spectrum can be used to define a characteristic wave period T. Furthermore the gravitational acceleration g is a parameter that enters both the definition of the energy flux in Eq. (3) as well as the dispersion relation, which for deep water waves is independent of depth. On dimensional grounds we suggest that a wave dependent characteristic length scale at the surface can be given by

$$l(z=0) = \gamma \sqrt{\frac{\Phi_{oc} T}{\rho_w g}}, \tag{17}$$

where γ is a non-dimensional constant. We have found that using $\gamma = 1$ for the Statfjord A case gives a length scale at $z = 0$ on the order of what was found by Gemmrich and Farmer (2004). To represent the characteristic period, we have chosen the mean period based on the first moment of the wave spectrum T_{m1} (Komen et al., 1994).

2.4 Particle dynamics

In this study we consider buoyant particles with a constant prescribed rise velocity w_r. The situation is analogous to the suspended sediments described by Burchard et al. (2008), except that the particles here have a positive buoyancy. The vertical distribution of the particle concentration C can be described by a suspended matter equation

$$\frac{\partial C}{\partial t} - \frac{\partial}{\partial z}\left(\nu_t' \frac{\partial C}{\partial z} - w_r C\right) = 0. \tag{18}$$

If the concentration is high enough, the mixing of particles will start to influence the TKE budget of the upper layer, in this study we will not consider such strong concentrations and neglect the influence of the buoyant particles on the mixing processes.

OSD
11, 1265–1300, 2014

2.5 Model and experimental setup

The mixing model used in our experiments is the General Ocean Turbulence Model (GOTM: for a description see Umlauf and Burchard, 2005), modified to take account of the wave effects described in the previous sections. Essentially, the momentum Eq. (6) are solved, with the upper boundary conditions in Eq. (8). The turbulence closure scheme is based on the solutions of the Eqs. (10) and (14), with upper boundary conditions given by Eqs. (13) and (17), respectively. For the bottom, zero flux boundary conditions are used.

In the experiments described below, the model has been run with rise velocities of $w_r = 50, 100, 200,$ and $400\,[\mathrm{m\,day^{-1}}]$, that could represent e.g. oil droplets of different size and/or chemical composition. Notably, $w_r = 100\,\mathrm{m\,day^{-1}}$ can also represent North East Arctic cod eggs (Sundby, 1983). For the results shown, the model has been run with the $k-\omega$ closure scheme, which performs well in the near surface layer (e.g. Umlauf et al., 2003; Jones and Monismith, 2008). For the $k-\omega$ scheme the exponents in Eq. (15) are given by $p = -1$, $m = 1/2$, $n = -1$. Each experiment has been run with: no wave forcing (control); adding only the Coriolis–Stokes force (C–S); adding only the wave breaking parametrization (TKE-injection); adding both (C–S + TKE-injection); and finally with also the Stokes shear production included (All).

3 Steady state balances

We start the model analysis with some idealized experiments to investigate the model behaviour for mixing and drift of buoyant particles. We focus on two cases: (i) a case with a rise velocity of $100\,\mathrm{m\,day^{-1}}$, and (ii) a case with a rise velocity of $400\,\mathrm{m\,day^{-1}}$. We consider a 500 m deep ocean column discretized using 300 grid points, with higher resolution close to the surface. For these experiments we use $f = 1.2\times10^{-4}\,\mathrm{s^{-1}}$, and a density of water $\rho_w = 1000\,\mathrm{kg\,m^{-3}}$. We consider steady state conditions, with varying wind speed directed along the x axis.

OSD
11, 1265–1300, 2014

In these idealized experiments the waves will be represented by a Pierson–Moscowitz spectrum (Pierson and Moskowitz, 1964). In principle, the stresses should be calculated using the wave spectra as described in Sect. 2.1, however, as we look on a steady-state situation the flux of momentum and energy is passing through the wave field and we therefore use a simple relation such that

$$\tau_x = \rho_w u_*^2 = \rho_a C_D U_{10}^2, \tag{19}$$

where ρ_a is the air density and C_D is the friction coefficient. Here we use $C_D = 1.5\times10^{-3}$ and $\rho_a = 1.2\,\mathrm{kg\,m^{-3}}$. Since we in this case use an empirical wave spectrum, we use the wave breaking parametrization of Craig and Banner (1994), using $\alpha = 100$. Since we use this parametrization of the energy flux, we do not relate the mixing length at the surface to the energy flux, and the boundary condition for the mixing length is given by Eq. (16). Following Umlauf and Burchard (2003) we use $L = 0.25$ and let $z_0 = H_S$.

3.1 Scaling analysis

To provide a tool for analyzing the model results we consider classical Ekman theory valid for a constant eddy viscosity, here denoted by A_z. The solutions to the classical Ekman problem are then given by (Ekman, 1905)

$$\begin{aligned} u &= V_0 \exp(z/D_E)\cos(\pi/4 + z/D_E), \\ v &= V_0 \exp(z/D_E)\sin(\pi/4 + z/D_E), \end{aligned} \tag{20}$$

where

$$\begin{aligned} V_0 &= u_*^2 \frac{1}{\sqrt{f\,A_z}}, \\ D_E &= \sqrt{\frac{2A_z}{f}}. \end{aligned} \tag{21}$$

OSD
11, 1265–1300, 2014

For A_z it is sometimes assumed that (e.g. Csanady, 1982)

$$A_z = \frac{u_*^2}{Xf}, \tag{22}$$

where X is a parameter and u_* is the (water side) friction velocity. Using Eq. (22) V_0 and D_E can be expressed as

$$\begin{aligned} V_0 &= \sqrt{X}u_*, \\ D_E &= \sqrt{\frac{2}{X}}\frac{u_*}{f}. \end{aligned} \tag{23}$$

Csanady (1982) finds that $X = 200$, while Rascle et al. (2006), who consider wave breaking use $X = 32$.

In a steady state, Eq. (18) reduces to

$$w_r \frac{\partial}{\partial z} C = \frac{\partial}{\partial z}\left(A_z \frac{\partial}{\partial z} C\right). \tag{24}$$

As boundary conditions we assume

$$C(z = 0) = C_0, C(z \to -\infty) \neq \infty. \tag{25}$$

The concentration is then given by

$$C(z) = C_0 \exp\left(\frac{z}{D_C}\right), \tag{26}$$

where $D_C = \frac{A_z}{w_r}$ is a characteristic concentration depth scale. The relation between the particle concentration and Ekman depth scales can then be expressed as

$$\frac{D_C}{D_E} = \frac{u_*}{w_r\sqrt{2X}}, \tag{27}$$

OSD
11, 1265–1300, 2014

which implies that the fraction D_C/D_E increases with the wind speed while it decreases with increasing particle rise speed. Interestingly, if both the friction velocity and the rise speed increases a given fraction, the fraction D_C/D_E remains constant. We notice that the factor X is important for the ratio, we do not aim at a detailed analysis of the value of X in this study, we have simply introduced the factor to be able to adjust curves such that a meaningful comparison between model results and scaling analysis can be made.

Another interesting quantity is the normalized transport velocity of particles defined as

$$\boldsymbol{u}_C = \frac{\int_{-D}^{0}(\boldsymbol{u}+\boldsymbol{u}_S)C(z)\mathrm{d}z}{\int_{-D}^{0}C(z)\mathrm{d}z} \tag{28}$$

For the scaling analysis we assume that $\boldsymbol{u}_S$ is zero (as it is not included in our analytical expressions). Analytical expressions that relates the transport to D_C and D_E can be found, however, here we do not consider these expressions as they do not provide simple insight into the dynamics of the transport velocity and direction. However, we find a useful relation between the x and y components, u_C and v_C, that can be described in simple terms as

$$v_C/u_C = -(1+2D_C/D_E), \tag{29}$$

we thus find that the transport of particles will have stronger veering when the particle concentration depth scale becomes larger. As an example we find that for a particle rise velocity of $100\,\mathrm{m\,day^{-1}}$, for a surface stress of roughly $0.05\,\mathrm{N\,m^{-2}}$, we have that $D_C = D_E$ and v_C/u_C increases by a factor 3 compared to the case when all particles are at the surface. The physical interpretation is simply that for deeper distribution of particles, the transport is dominated by the currents deeper down into the Ekman layer, which in turn has stronger veering.

OSD
11, 1265–1300, 2014

3.2 Transport and vertical distribution of particles

For the evaluation of the model results, we define the Ekman and the characteristic concentration depth scales from the model as

$$D_{\mathrm{E}}^{(m)} = \frac{\int_{-D}^{0} |\boldsymbol{u}| \, \mathrm{d}z}{|\boldsymbol{u}(z=0)|}, D_{\mathrm{C}}^{(m)} = \frac{\int_{-D}^{0} C(z) \, \mathrm{d}z}{C(z=0)}. \quad (30)$$

The model results for these variables are shown in Fig. 1. Also shown as horizontal lines are the solutions predicted by Eq. (23), for $X = 32$ and $X = 200$. While the model result approaches the solution $X = 200$ in the case when no wave effects are included, the results when wave mixing is included are closer to $X = 32$. This difference is consistent with the previous discussion that without wave effects $X = 200$ has been used (Csanady, 1982), while $X = 32$ has been used for the wave breaking case (Craig and Banner, 1994; Rascle et al., 2006). From simple scaling theory Eq. (23) we expect that the velocity at the surface and the Ekman depth should vary approximately linearly with the friction velocity (or that the scaled Ekman depth should be constant), but as seen in Fig. 1 the solutions are far from linear. We also see that the cases with wave breaking is further from the scaling law, suggesting that the additional flux of TKE from waves breaks the original assumptions in the scaling theory. Nevertheless, the scaling laws, and the model deviation from the scaling laws, still provide some insight into the dynamics of the system. Especially we see that the cases with wave breaking are quite different from the cases without wave breaking, and show very different asymptotic behaviour. For the normalized characteristic particle depth (i.e. $D_{\mathrm{C}}/D_{\mathrm{E}}$) we find that it increases as u_*, or as the square root of the stress, from the scaling analysis. However, taking into account that the mixing is parabolic with depth in a non-stratified ocean, we do expect that the model $D_{\mathrm{C}}/D_{\mathrm{E}}$ should lie below the scaling law when $D_{\mathrm{C}}/D_{\mathrm{E}}$ is smaller than unity and above the scaling law when $D_{\mathrm{C}}/D_{\mathrm{E}}$ is larger than unity. This is illustrated in Fig. 2. Only the cases where the waves are completely neglected and the case with all wave effects are shown. It may be noted that here we

OSD
11, 1265–1300, 2014

have adjusted the value of X such that the scaling law fits the model for $D_C/D_E = 1$. One interesting feature we notice is that for low rise velocities, the particles are mixed very deep, indicating that the eddy viscosity is quite high even below the region where the Reynolds stresses are important (i.e., the Ekman layer depth). This means that the weak turbulent velocities must be compensated by a large mixing length scale.

From the scaling laws Eqs. (27) and (29) we expect that the mean transport velocity of the particles will veer as we increase the wind stress, and this is clearly seen in Fig. 3. We notice that the model does not have as strong veering as predicted by the scaling law, and this is most likely explained by the fact that the eddy viscosity is far from constant in the model. We see that results are closer for a low rise velocity than for a high rise velocity. This is in agreement with the results of the scaling depths for momentum (D_E) and particles (D_C) as discussed earlier. We also see that cases with all wave effects included have a stronger veering in particle drift than the model without waves, consistent with our expectations that waves mix particles deeper and also create a stronger veering due to the Coriolis–Stokes force. So far we have mainly considered non-dimensionalized drift velocities, and the translation to real situations requires a dimensionalization of the results. For more accessible results we plot the drift speed scaled by the wind speed at ten meters height and the angle, θ, between the drift direction and the wind direction in Figs. 4 and 5. When the waves are not included, the total momentum must be contained in the Eulerian current, while when the waves are included, the Stokes drift is added. From the mean particle drift it can be seen that in all cases this relation approaches a constant value, which notably is much lower than the 3% value that is often used in the empirical relation Eq. (1) for surface drift. In agreement with earlier discussion, we also see that the veering increases with increasing wind speed and that cases with all wave effects has stronger veering than the standard model setup.

OSD
11, 1265–1300, 2014

4 Statfjord A oil spill

4.1 Environmental conditions

The Statfjord A oilfield is located approximately at 61.25° N 1.85° E about 200 km off the western coast of Norway, in an area with rather steep bottom slopes (Fig. 6). This was the site of a large oil spill in December 2007 (Broström et al., 2008). Starting on the 12 December 2007 08:17 UTC and lasting for 20–45 min, an estimated 4400 m^3 of crude oil was spilled into the ocean from a ruptured loading hose near the platform. Since the wind and wave conditions were quite severe during and after the spill (see Fig. 7), few observations of the oil slick exist. After a few hours the slick was estimated to be 8 km long and 1 km wide, and by late afternoon on 12 December its surface area covered an estimated 23 km^3. The only observation of the oil slick from aircraft was made two days later, on the 14 December at 13:48 UTC. Located approximately 16 km to the east-southeast of the spill site, the slick was then about 10 km long and 5 km wide. As a simple rule of thumb it is often taken that the drift of floating objects is approximately 3 % of the wind speed and 15° to the right of the wind direction (Hackett et al., 2006). While such estimates, which can be expressed through Eq. (1), may apply for oil drift in light wind conditions and calm seas (Reed et al., 1999), the situation is quite different in cases with more severe weather like the Statfjord A accident. In this case the drift was closer to 0.5 % of the wind speed and about 90–120° to the right.

For the results in this case study the model has been run with wind and wave forcing from the ERA-Interim reanalysis (Dee et al., 2011). In Fig. 7 it can be seen that the wind was essentially towards north and around 15 $m\,s^{-1}$ for about two days following the accident, and the significant wave height H_S was up to 4.5 m. Also shown in Fig. 7 is the surface Stokes drift direction and magnitude. The time from the oil spill started to the observation two days later coincides with a peak in momentum and energy fluxes into the ocean (Fig. 7).

OSD
11, 1265–1300, 2014

For hydrography we use observations available from the International Council for the Exploration of the Sea (ICES). Typical for the area and time of the year, the observations show very little stratification.

In this area there is a branch of Atlantic water flowing along the bottom contours (e.g. Albretsen and Røed, 2010, Fig. 9). To make an estimate of this current component we have used the model hindcast archive described by Lien et al. (2013). The approximate magnitude and direction is illustrated by the daily mean at 100 m depth on the 13 December 2007 in Fig. 6. While the wind driven current and the Stokes drift decay with depth, the topographic current extends over most of the water column, so the relative importance of the different current components on the transport depends on the depth of the particles.

4.2 Transport and vertical distribution of particles

An example of how the wave effects modify the Eulerian currents (12 December 2007 21:00 UTC) can be seen in Fig. 8. As can be expected from previous studies (e.g. Polton et al., 2005), the Coriolis–Stokes force turns the current further to the right. In all cases when wave effects are included the sea state dependent momentum flux is calculated using Eq. (4). The wave breaking parametrization has a large impact on the velocities close to the surface, while the Stokes shear production in this case is less important for the upper ocean mixing. When all wave effects are included the surface current speed is reduced by more than 50 %.

Comparing concentration profiles for the cases with and without waves (Fig. 9), it can be seen that the waves increase the mixing. In general the increased mixing by the waves lead to a higher concentration of particles deeper down in the water masses. Hence, the currents deeper down become more important for the net transport when wave induced mixing is included. Furthermore, it can be seen that the wave effects are more important for higher rise velocities w_r: for low w_r the shear turbulence is sufficient to mix the particles down and hence profiles with and without waves are more similar. While the wind and wave conditions cause strong mixing in the beginning of the

OSD
11, 1265–1300, 2014

accident, the calmer conditions from approximately 40 h into the spill cause more and more particles to resurface until the time of the observation about 53 h after the spill. With the current $\boldsymbol{u}$ and the relative concentration profiles $C(z)$ from the mixing model, the background current $\boldsymbol{u}_{\mathrm{BG}}$ estimated from the model hindcast of Lien et al. (2013), and the Stokes drift $\boldsymbol{u}_{\mathrm{S}}$ calculated from the wave spectra, a transport velocity similar to Eq. (28) can be defined as

$$\boldsymbol{u}^{(m)} = \frac{\int_{-D}^{0}(\boldsymbol{u} + \boldsymbol{u}_{\mathrm{BG}} + \boldsymbol{u}_{\mathrm{S}})C(z)\,\mathrm{d}z}{\int_{-D}^{0}C(z)\,\mathrm{d}z}. \tag{31}$$

Using this, the transport of particles by the model can be compared with the observation, and the result is shown in Fig. 10. While the direction of the predicted oil spill coincides quite nicely with the observation, the modeled drift seems to be too fast. Depending on the rise velocities, the end locations from the model spread in a southwest-northeast direction, similar to the observed oil slick. Also shown in Fig. 10 are two different end locations predicted when using the empirically based relation Eq. (1). One is the expected drift of oil at the surface, with a speed of 3 % of the wind speed at an angle of 15° to the right (Reed et al., 1999; Hackett et al., 2006), while the other is based on observations that oil that is mixed below the surface has a mean drift of 1 % of the wind speed with an angle of 90° to the right (Reed et al., 1994). The background current has a significant effect on both the modelled drift using Eq. (31) and when using the empirical relation Eq. (1). On average the magnitude of $\boldsymbol{u}_{\mathrm{BG}}$ is about 50 % of the surface value of the combined wind driven and Stokes drift components. Here we consider the background current to be the least known, but a more detailed analysis is beyond the scope of the present study.

OSD
11, 1265–1300, 2014

5 Concluding remarks

The results from the steady state analysis and the Statfjord A oil spill case indicate that the wave breaking parametrization is the most influential wave effect for the mixing and transport of buoyant particles. In the Statfjord A case presented above, the increased mixing is mainly a result of the injection of TKE through the boundary condition Eq. (13). Wave breaking parametrizations like the one presented in this study is justified by measurements of increased levels of dissipation rate, ε, beneath breaking waves (e.g. Agrawal et al., 1992). Such observations have led to several studies proposing scaling laws of ε other than the classic law of the wall (Anis and Moum, 1995; Terray et al., 1996; Huang and Qiao, 2010). While these scaling laws are shown to give a better representation of ε in several cases, there are some observations (e.g. Sutherland et al., 2013, 2014) that show better agreement with the law of the wall scaling of ε. The drift of oil in the Statfjord A case is similar to two oil release experiments in 1991, which are two of four experiments considered by Reed et al. (1994). In those cases the oil moved with a mean speed of about 1% of the wind speed, virtually 90° to the right of the wind direction, and a qualitative explanation is given by Reed et al. (1994). During the Statfjord A accident, the mean drift of the oil was significantly slower relative to the wind at about 0.5% of the wind speed, and slightly further deflected away from the wind direction. This difference may in part be due to higher wind speed during the Statfjord A oil spill, which leads to increased mixing. Although the deflection and decrease in drift is partly due to strong ocean currents in the area, the results from the Statfjord A case show that the waves play a significant role in the drift. Our results indicate that the most important wave induced mechanism for the drift is the injection of TKE from breaking waves. The increased mixing of particles into the water column result in a slower drift, veering towards the right (Northern Hemisphere) and the background currents become more important. The theory described contributes to give physical understanding of the observed drift, and the model results show some of the potential effects of waves in drift modelling.

OSD
11, 1265–1300, 2014

Acknowledgements. We gratefully acknowledge financial support from the Research Council of Norway through grants 196438 (BioWave), 20754 (OilWave) and the European Union/FP7 through grant 284455 (MyWave).

References

Agrawal, Y. C., Terray, E. A., Donelan, M. A., Hwang, P. A., Williams, A. J., Drennan, W., Kahma, K., and Kitaigorodskii, S.: Enhanced dissipation of kinetic energy beneath surface waves, Nature, 359, 219–220, doi:10.1038/359219a0, 1992. 1268, 1285

Albretsen, J. and Røed, L. P.: Decadal long simulations of mesoscale structures in the northern North Sea/Skagerrak using two ocean models, Ocean Dynam., 60, 933–955, 2010. 1283

Andrews, D. and McIntyre, M.: An exact theory of nonlinear waves on a Langrangian-mean flow, J. Fluid Mech., 89, 609–646, 1978. 1268

Anis, A. and Moum, J. N.: Surface wave-turbulence interactions: scaling $\epsilon(z)$ near the sea surface, J. Phys. Oceanogr., 25, 2025–2045, 1995. 1285

Ardhuin, F. and Jenkins, A. D.: On the interaction of surface waves and upper ocean turbulence, J. Phys. Oceanogr., 36, 551–557, doi:10.1175/JPO2862.1, 2006. 1268

Broström, G., Carrasco, A., Hackett, B., and Saetra, Ø.: Using ECMWF products in global marine drift forecasting services, ECMWF Newsletter, 118, 16–20, 2008. 1282

Burchard, H., Flöser, G., Staneva, J. V., Badewien, T. H., and Riethmüller, R.: Impact of density gradients on net sediment transport into the Wadden Sea, J. Phys. Oceanogr., 38, 566–587, 2008. 1275

Carniel, S., Warner, J. C., Chiggiato, J., and Sclavo, M.: Investigating the impact of surface wave breaking on modeling the trajectories of drifters in the northern Adriatic Sea during a wind-storm event, Ocean Model., 30, 225–239, 2009. 1274

Craig, P. D. and Banner, M. L.: Modelling Wave-Enhanced Turbulence in the Ocean Surface Layer, J. Phys. Oceanogr., 24, 2546–2559, 1994. 1268, 1270, 1274, 1277, 1280

Craik, A.: The generation of Langmuir circulations by an instability mechanism, J. Fluid Mech., 81, 209–223, 1977. 1268

Csanady, G. T.: Circulation in the Coastal Ocean, Vol. 2, Springer, 1982. 1278, 1280

OSD
11, 1265–1300, 2014

Dee, D. P., Uppala, S. M., Simmons, A. J., Berrisford, P., Poli, P., Kobayashi, S., Andrae, U., Balmaseda, M. A., Balsamo, G., Bauer, P., Bechtold, P., Beljaars, A. C. M., van de Berg, L., Bidlot, J., Bormann, N., Delsol, C., Dragani, R., Fuentes, M., Geer, A. J., Haimberger, L., Healy, S. B., Hersbach, H., Holm, E. V., Isaksen, L., Kallberg, P., Kohler, M., Matricardi, M., McNally, A. P., Monge-Sanz, B. M., Morcrette, J.-J., Park, B.-K., Peubey, C., de Rosnay, P., Tavolato, C., Thepaut, J.-N., and Vitart, F.: The ERA-Interim reanalysis: configuration and performance of the data assimilation system, Q. J. Roy. Meteor. Soc., 137, 553–597, 2011. 1269, 1282

Ekman, V. W.: On the influence of the earth's rotation on ocean currents, Ark. Mat. Astron. Fys., 2, 1–53, 1905. 1277

Gemmrich, J., Mudge, T., and Polonichko, V.: On the energy input from wind to surface waves, J. Phys. Oceanogr., 24, 2413–2417, 1994. 1268

Gemmrich, J. R. and Farmer, D. M.: Observations of the scale and occurrence of breaking surface waves, J. Phys. Oceanogr., 29, 2595–2606, 1999. 1274

Gemmrich, J. R. and Farmer, D. M.: Near-surface turbulence in the presence of breaking waves, J. Phys. Oceanogr., 34, 2004. 1274, 1275

Grant, A. L. M. and Belcher, S. E.: Characteristics of langmuir turbulence in the ocean mixed layer, J. Phys. Oceanogr., 39, 1871–1887, 2009. 1272

Hackett, B., Breivik, Ø., and Wettre, C.: Forecasting the drift of objects and substances in the ocean, in: Ocean Weather Forecasting, edited by: Chassignet, E. and Verron, J., 507–523, Springer Netherlands, doi:10.1007/1-4020-4028-8_23, 2006. 1266, 1267, 1282, 1284

Huang, C. J. and Qiao, F.: Wave-turbulence interaction and its induced mixing in the upper ocean, J. Geophys. Res.-Oceans, 115, C04026, doi:10.1029/2009JC005853, 2010. 1268, 1285

James, I.: Modelling pollution dispersion, the ecosystem and water quality in coastal waters: a review, Environ. Modell. Softw., 17, 363–385, 2002. 1266

Janssen, P. A. E. M.: Ocean wave effects on the daily cycle in SST, J. Geophys. Res., 117, C00J32, doi:10.1029/2012JC007943, 2012. 1267, 1268, 1270, 1271

Jenkins, A. D.: The use of a wave prediction model for driving a near-surface current model, Deutsche Hydrografische Zeitschrift, 42, 133–149, doi:10.1007/BF02226291, 1989. 1271

Johansen, Ø.: DeepBlow – a lagrangian plume model for deep water blowouts, Spill Sci. Technol. B., 6, 103–111, 2000. 1267

OSD
11, 1265–1300, 2014

Jones, N. L. and Monismith, S. G.: Modeling the influence of wave-enhanced turbulence in a shallow tide-and wind-driven water column, J. Geophys. Res.-Oceans, 113, C03009, doi:10.1029/2007JC004246, 2008. 1274, 1276

Kantha, L. and Clayson, C. A.: On the effect of surface gravity waves on mixing in the oceanic mixed layer, Ocean Model., 6, 101–124, 2004. 1268

Kantha, L., Lass, H. U., and Prandke, H.: A note on Stokes production of turbulence kinetic energy in the oceanic mixed layer: observations in the Baltic Sea, Ocean Dynam., 60, 171–180, 2010. 1268

Komen, G., Caveleri, L., Donelan, M., Hasselmann, K., and Janssen, P. A. E. M.: Dynamics and Modelling of Ocean Waves, Cambridge University Press, 1994. 1270, 1275

Lewis, D. and Belcher, S.: Time-dependent, coupled, Ekman boundary layer solutions incorporating Stokes drift, Dynam. Atmos. Oceans, 37, 313–351, 2004. 1267

Lien, V. S., Gusdal, Y., Albretsen, J., Melsom, A., and Vikebø, F. B.: Evaluation of a Nordic Seas 4 km numerical ocean model hindcast archive (SVIM), 1960–2011, Tech. Rep. 7, Institute of marine research, fisken og havet, available at: http://www.imr.no/filarkiv/2014/01/fh_7-2013_swim_til_web.pdf/en (last access: 17 January 2014), 2013. 1283, 1284, 1296

Paskyabi, M. B. and Fer, I.: Turbulence structure in the upper ocean: a comparative study of observations and modeling, Ocean Dynam., 64, 611–631, 2014. 1268

Pierson, W. J. and Moskowitz, L.: A proposed spectral form for fully developed wind seas based on the similarity theory of SA Kitaigorodskii, J. Geophys. Res., 69, 5181–5190, 1964. 1277

Polton, J. A., Lewis, D. M., and Belcher, S. E.: The role of wave-induced Coriolis–Stokes forcing on the wind-driven mixed layer, J. Phys. Oceanogr., 35, 444–457, doi:10.1175/JPO2701.1, 2005. 1267, 1271, 1283

Rascle, N. and Ardhuin, F.: Drift and mixing under the ocean surface revisited: stratified conditions and model-data comparisons, J. Geophys. Res., 114, C02016, doi:10.1029/2007JC004466, 2009. 1274

Rascle, N., Ardhuin, F., and Terray, E. A.: Drift and mixing under the ocean surface: a coherent one-dimensional description with application to unstratified conditions, J. Geophys. Res.-Oceans, 111, C03016, doi:10.1029/2005JC003004, 2006. 1278, 1280

Rascle, N., Chapron, B., Ardhuin, F., and Soloviev, A.: A note on the direct injection of turbulence by breaking waves, Ocean Model., 70, 145–151, doi:10.1016/j.ocemod.2012.09.001, 2012. 1274

OSD
11, 1265–1300, 2014

Reed, M., Turner, C., and Odulo, A.: The role of wind and emulsification in modelling oil spill and surface drifter trajectories, Spill Sci. Technol. B., 1, 143–157, 1994. 1267, 1284, 1285

Reed, M., Johansen, Ø., Brandvik, P. J., Daling, P., Lewis, A., Fiocco, R., Mackay, D., and Prentki, R.: Oil spill modeling towards the close of the 20th century: overview of the state of the art, Spill Sci. Technol. B., 5, 3–16, 1999. 1267, 1282, 1284

Röhrs, J., Christensen, K. H., Hole, L. R., Broström, G., Drivdal, M., and Sundby, S.: Observation-based evaluation of surface wave effects on currents and trajectory forecasts, Ocean Dynam., 62, 1519–1533, 2012. 1268

Saetra, Ø., Albretsen, J., and Janssen, P. A. E. M.: Sea-state-dependent momentum fluxes for ocean modeling, J. Phys. Oceanogr., 37, 2714–2725, 2007. 1267, 1271, 1274

Sundby, S.: A one-dimensional model for the vertical distribution of pelagic fish eggs in the mixed layer, Deep-Sea Res. Pt. I, 30, 645–661, 1983. 1276

Sutherland, G., Ward, B., and Christensen, K. H.: Wave-turbulence scaling in the ocean mixed layer, Ocean Sci., 9, 597–608, doi:10.5194/os-9-597-2013, 2013. 1268, 1285

Sutherland, G., Christensen, K., and Ward, B.: Evaluating Langmuir turbulence parameterizations in the ocean surface boundary layer, J. Geophys. Res.-Oceans, 119, 1899–1910, doi:10.1002/2013JC009537, 2014. 1268, 1285

Terray, E. A., Donelan, M. A., Agrawal, Y. C., Drennan, W. M., Kahma, K. K., Williams, A. J., Hwang, P. A., and Kitaigorodskii, S. A.: Estimates of kinetic energy dissipation under breaking waves, J. Phys. Oceanogr., 26, 792–807, doi:10.1175/1520-0485(1996)026<0792:EOKEDU>2.0.CO;2, 1996. 1268, 1285

Umlauf, L. and Burchard, H.: A generic length-scale equation for geophysical turbulence models, J. Mar. Res., 61, 235–265, 2003. 1273, 1274, 1277

Umlauf, L. and Burchard, H.: Second-order turbulence closure models for geophysical boundary layers. A review of recent work, Cont. Shelf. Res., 25, 795–827, 2005. 1276

Umlauf, L., Burchard, H., and Hutter, K.: Extending the k–ω model towards oceanic applications, Ocean Model., 5, 195–218, 2003. 1274, 1276

Ursell, F.: On the theoretical form of ocean swell. On a rotating earth, Monthly Notices Roy. Astron. Soc., 6, 1–8, 1950. 1267

Warner, J. C., Sherwood, C. R., Arango, H. G., and Signell, R. P.: Performance of four turbulence closure models implemented using a generic length scale method, Ocean Model., 8, 81–113, 2005. 1274

OSD
11, 1265–1300, 2014

Weber, J. E. H.: A note on mixing due to surface wave breaking, J. Geophys. Res.-Oceans, 113, C11009, doi:10.1029/2008JC004758, 2008. 1268
Weber, J. E. H., Broström, G., and Saetra, Ø.: Eulerian versus Lagrangian approaches to the wave-induced transport in the Upper Ocean, J. Phys. Oceanogr., 36, 2106–2118, 2006. 1267

OSD
11, 1265–1300, 2014

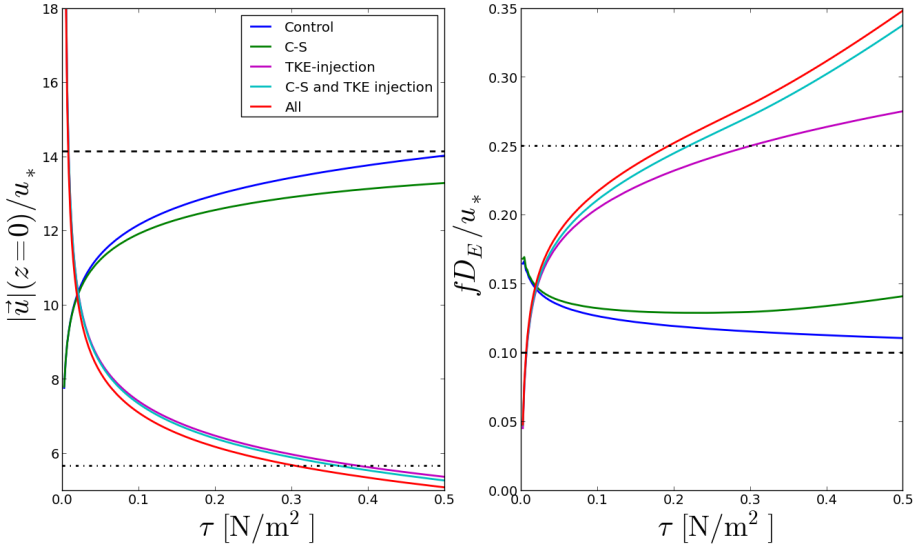

Figure 1. The normalized velocity at the surface as a function of the wind stress (left). Normalized Ekman depth as a function of the wind stress (right). The horizontal black lines represent the solutions predicted by Ekman theory for $X = 200$ (dashed line) and for $X = 32$ (dash-dotted line).

OSD
11, 1265–1300, 2014

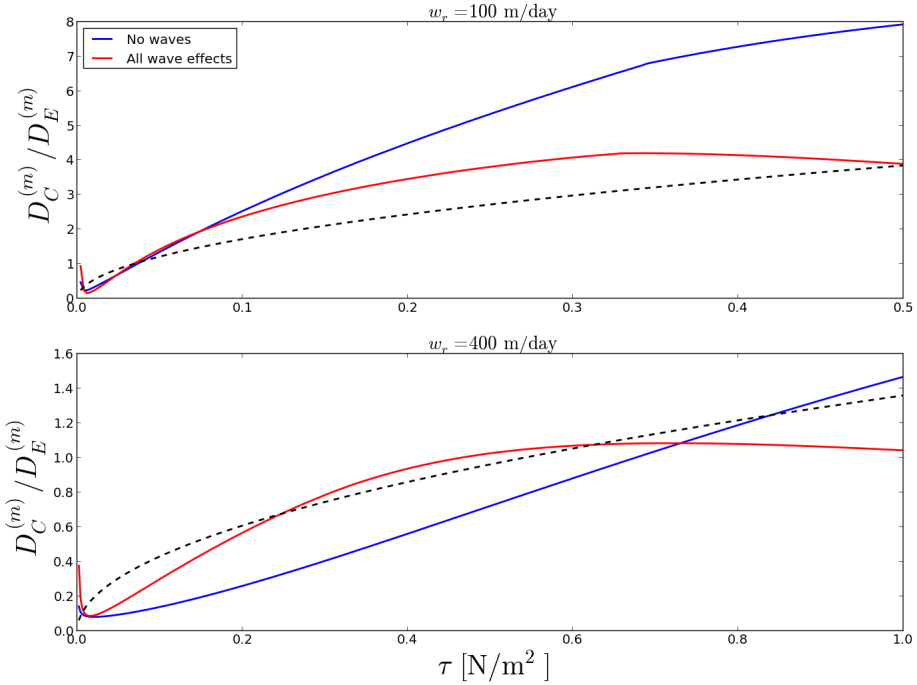

Figure 2. The normalized particle depth ($D_C^{(m)}/D_E^{(m)}$) for rise velocities of w_r = 100 m day^{-1} (top panel) and w_r = 400 m day^{-1} (bottom panel). Note the difference in scale of the axes.

OSD
11, 1265–1300, 2014

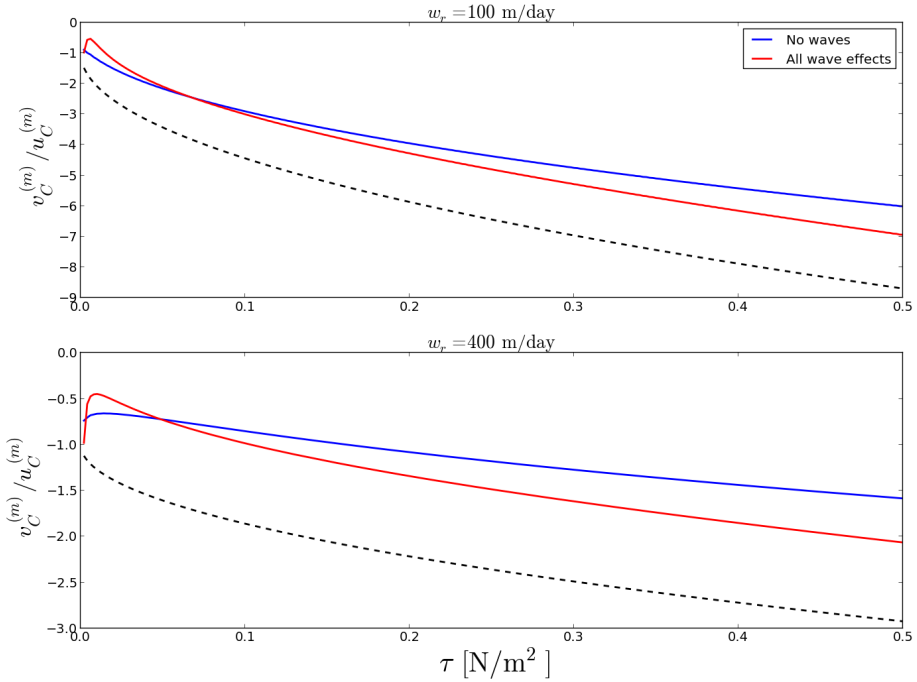

Figure 3. The *y* velocity scaled by the *x* velocity as a function of wind stress for rise velocities of w_r = 100 m day^{-1} (top panel) and w_r = 400 m day^{-1} (bottom panel).

OSD
11, 1265–1300, 2014

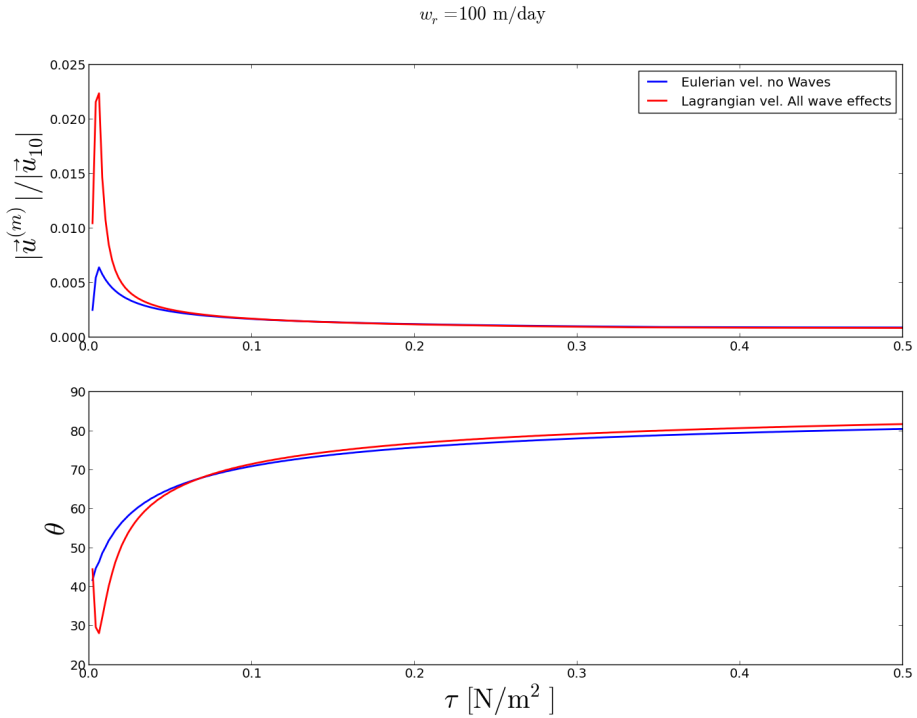

Figure 4. Particle transport speed relative to the wind speed at 10 m (top) and the angle, θ, between the transport velocity and the wind (bottom). The rise velocity is w_r = 100 m day^{-1}.

OSD
11, 1265–1300, 2014

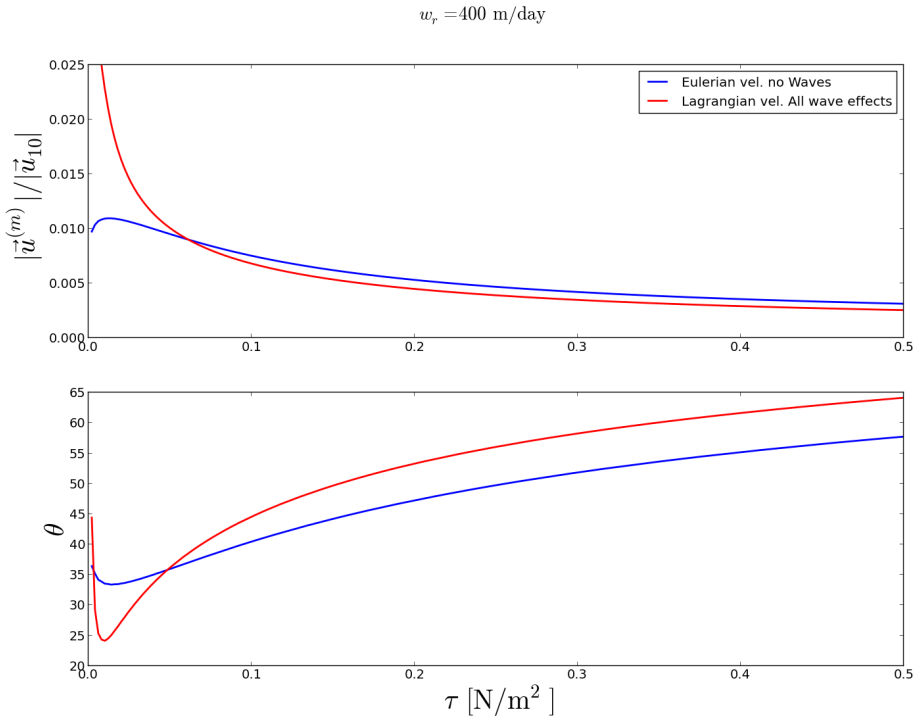

Figure 5. Same as Fig. 4, but for particle rise velocity of 400 m day^{-1}.

OSD
11, 1265–1300, 2014

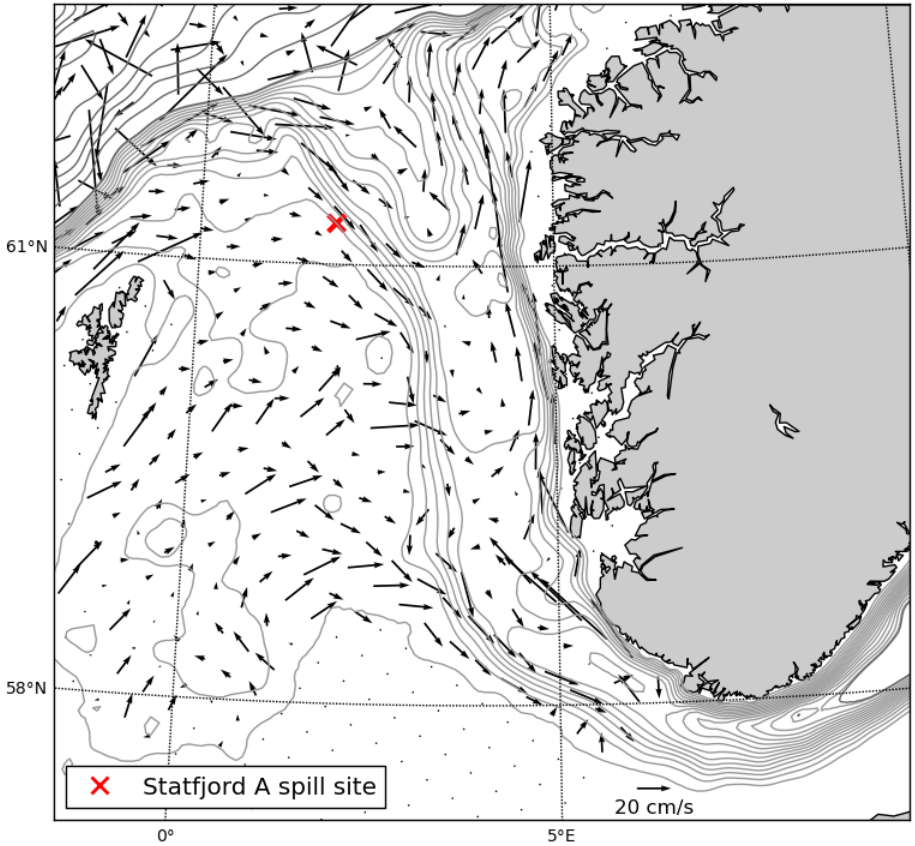

Figure 6. Statfjord A area with bottom contours and currents (daily mean 13 December 2007) at 100 m depth from SVIM hindcast archive (Lien et al., 2013).

OSD
11, 1265–1300, 2014

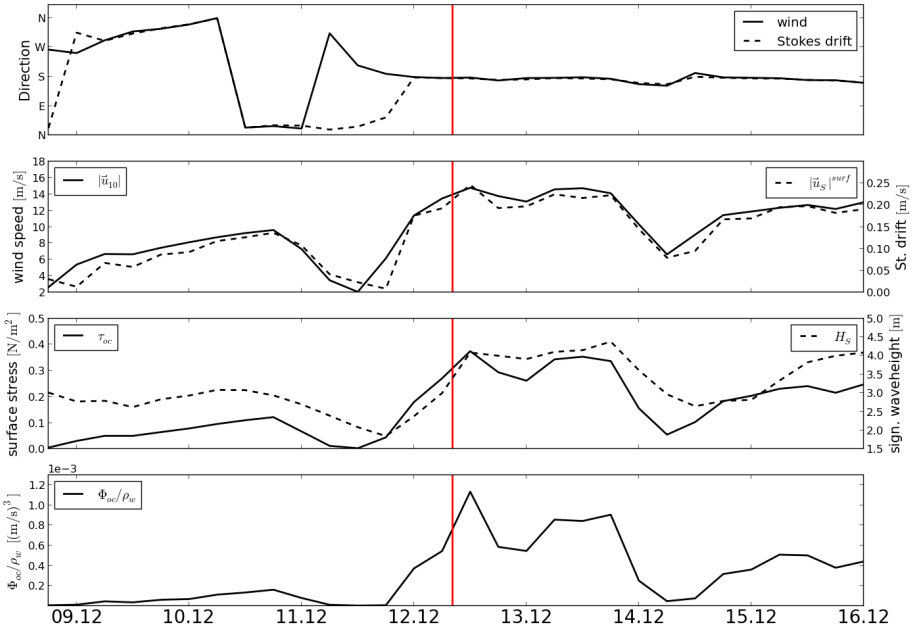

Figure 7. Wind and wave conditions from ERA Interim before, during and after the Statfjord A oil spill. The incident time of the oil spill is indicated by the vertical red line.

OSD
11, 1265–1300, 2014

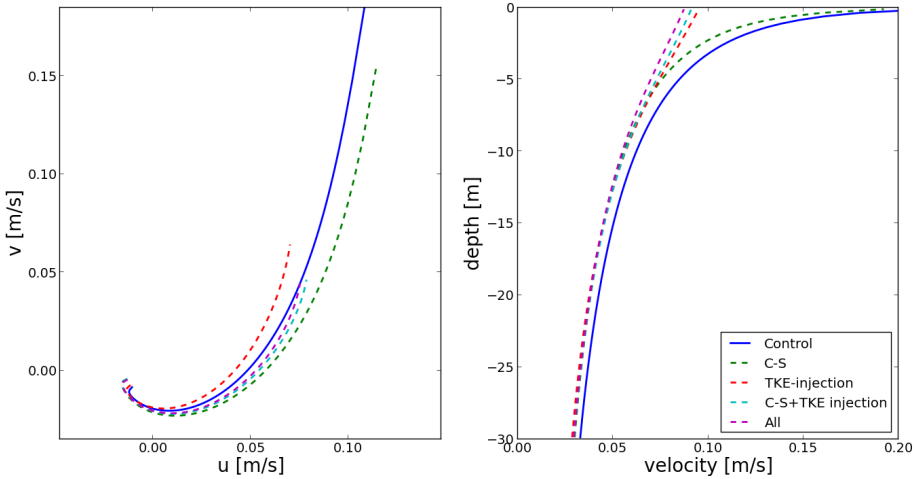

Figure 8. Hodograph (left) and depth profile (right) of the Eulerian current approximately 12 h after oil spill (12 December 2007 21:00).

OSD
11, 1265–1300, 2014

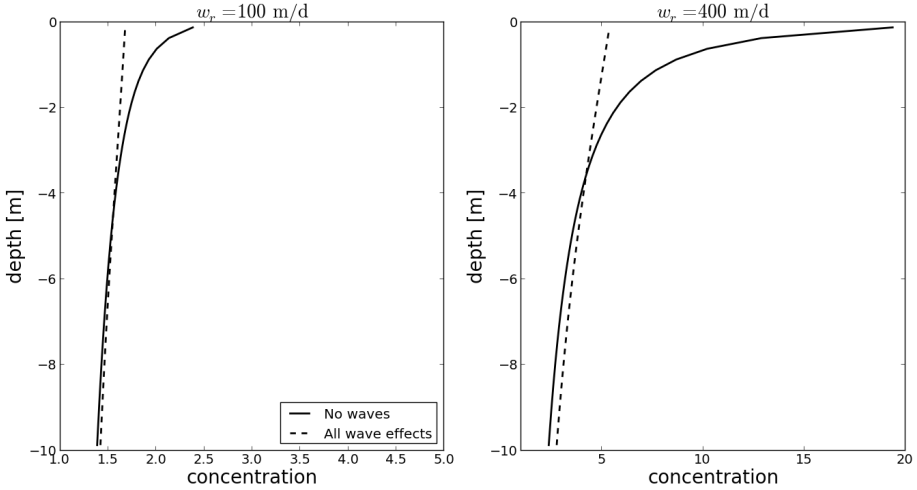

Figure 9. Concentration profile approximately 12 h after the oil spill (12 December 2007 21:00) for particles with rise velocity of 100 m day^{-1} (left) and 400 m day^{-1} (right). Note the difference in scale of the x axis.

OSD
11, 1265–1300, 2014

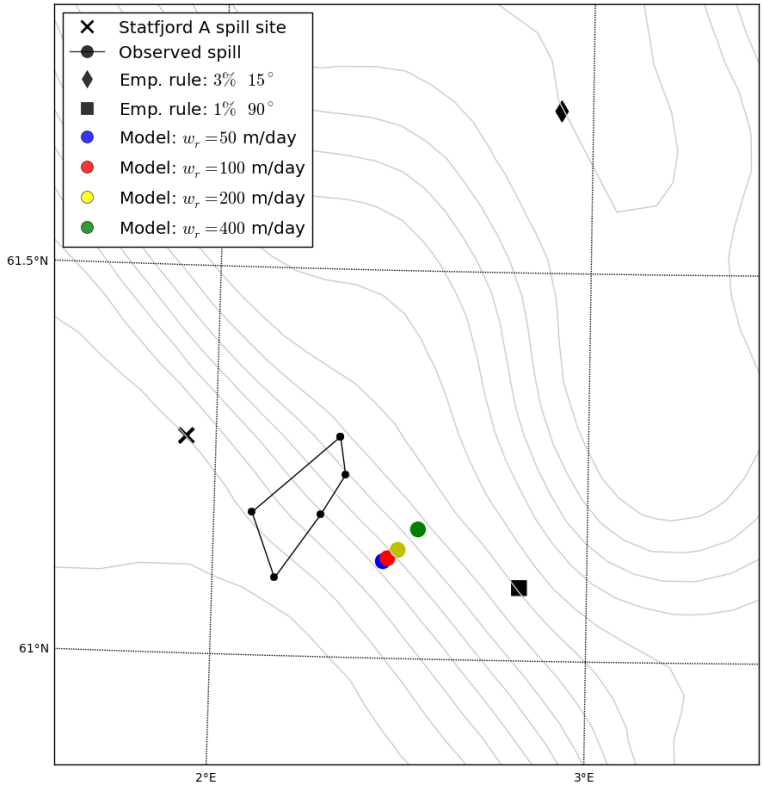

Figure 10. Mean location of oil predicted by the model for different rise velocities of the particles. Also shown is the mean locations predicted by empirically based relations between the drift and the wind vector. The observed oil slick is shown with coordinates from observation (14 December 2007 13:48 UTC) connected with lines.

OSD
11, 1265–1300, 2014